Journal of Alloys and Compounds 508 (2010) 629–635

Contents lists available at ScienceDirect

Journal of Alloys and Compounds

journal homepage: www.elsevier.com/locate/jallcom

Hydrothermal synthesis and electrochemical properties of nano-sized Co–Sn alloy anodes for lithium ion batteries

Jianchao He[a], Hailei Zhao[a,b,*], Jing Wang[a], Jie Wang[a], Jingbo Chen[a]

[a] School of Material Science and Engineering, University of Science and Technology Beijing, Beijing 100083, China
[b] Beijing Key Lab of New Energy Materials and Technology, Beijing 100083, China

ARTICLE INFO

Article history:
Received 18 June 2010
Received in revised form 24 August 2010
Accepted 25 August 2010
Available online 9 September 2010

Keywords:
Co–Sn alloy
Anode
Hydrothermal route
Mechanism
Lithium ion battery

ABSTRACT

Nano-sized Co–Sn alloys with a certain amount of Sn oxides used as potential anode materials for lithium ion batteries were synthesized by hydrothermal route. The effects of hydrothermal conditions and post annealing on the phase compositions and the electrochemical properties of synthesized powders were characterized by means of X-ray diffraction (XRD), field-emission scanning electron microscopy (FESEM) with energy dispersive spectra (EDS) analysis and galvanostatic cycling tests. Prolonging the dwelling time at the same hydrothermal temperature can increase the content of Sn oxides, which will lead to a high initial irreversible capacity loss but a better cycling stability owing to the buffer effect of irreversible product Li_2O. Heat-treatment can increase the crystallinity and cause the presence of a certain amount of inert CoSn component, which both have positive impact on the cycling stability of Co–Sn electrode. By comparison with the lithiation/delithiation processes of metal Sn, a two-step mechanism of $CoSn_2$ alloy during cycling was confirmed.

1. Introduction

Recently, there has been substantial interest in Sn-based alloys in order to replace carbonaceous materials as anode electrode in lithium ion batteries. The Sn-based alloys possess high specific energy densities and relatively safe lithiation/delithiation voltages, however, the mechanical fatigue caused by large volume change during lithium intercalation and extraction processes remains their most important challenge to be used as anodes in lithium ion batteries. To obtain long-lived anode materials, nanostructured Sn-based alloys have recently attracted much interest [1–3]. Compared with fully crystalline counterparts, the structural features of nanocrystals could offer short path length for electronic and cation transports and higher electrode active specific area, which can result in higher capacity and better rate capability [1].

Hydrothermal route, with respect to the relative simplicity and prominent flexibility, is recognized as a powerful technique for the preparation of a variety of nanostructured amorphous and crystalline Sn-based alloys, including Co–Sn alloys [4–7], Fe–Sn alloys [8] and Sn–Sb alloys [9,10]. These alloy materials showed better cyclic performance than the comparable ones prepared by mechanic melting method [6,9] and chemical reduction process [8]. However, there is limited report in the literature concerning the detailed reaction process of hydrothermal route for the synthesis of Sn-based alloy anodes and the effect of variation in hydrothermal conditions on the structure and electrochemical properties of obtained Sn-based alloys.

Co–Sn alloy exhibits high specific capacity and good cycling performance, and thus being a promising anode alternative for lithium ion batteries [11]. The motivation of this contribution is to inspect the reaction process of hydrothermal route for the synthesis of Co–Sn alloy anode and clarify the effect of dwelling time and post-annealing on the electrodes electrochemical properties. The lithiation/delithiation mechanism of Co–Sn alloy is also discussed. The detailed investigation in this work provides the possible strategies to improve further the electrochemical performance of Co–Sn alloy anode in the future work.

2. Experimental

Analytically pure $CoCl_2{\cdot}6H_2O$ (≥99.0%) and $SnCl_2{\cdot}2H_2O$ (≥98.0%) were used as the starting materials in the hydrothermal synthesis. The starting materials in the atomic ratio of 1:3 to Co:Sn were put into a Teflon-lined autoclave, which was then filled with de-ionized water up to 80% of its volume. The concentrations of $CoCl_2{\cdot}6H_2O$ and $SnCl_2{\cdot}2H_2O$ in the resulted solutions are 0.06 M and 0.18 M, respectively. After adding slowly sufficient $NaBH_4$ (≥96.0%) as the reductant, according to reaction (1), the obtained solution was sealed in a Teflon-lined autoclave and heated to 160 °C for 24 h, 48 h and 60 h, respectively, to investigate the effect of dwelling time at a certain temperature on the phase composition and the electrochemical properties of Co–Sn alloy powders. After reaction, the autoclave was cooled down to room temperature naturally. The precipitate was filtered, washed with ethanol and distilled water several times, and dried under vacuum at 120 °C for 8 h. The final

* Corresponding author at: School of Materials Science and Engineering, University of Science and Technology, Beijing 100083, China. Tel.: +86 10 82376837; fax: +86 10 82376837.
E-mail address: hlzhao@ustb.edu.cn (H. Zhao).

0925-8388/$ – see front matter © 2010 Elsevier B.V. All rights reserved.
doi:10.1016/j.jallcom.2010.08.152

Table 1
Synthesis conditions of the samples investigated in this work.

Sample label	Nominal composition	Hydrothermal temperature	Dwelling time	Annealing temperature	Annealing time
A0	$CoSn_3$	\	\	\	\
A1	$CoSn_3$	160 °C	24 h	\	\
A2	$CoSn_3$	160 °C	48 h	\	\
A3	$CoSn_3$	160 °C	60 h	\	\
A4	$CoSn_3$	160 °C	48 h	500 °C	2 h
A5	Sn	160 °C	48 h	\	\

products were labeled as samples A1, A2 and A3, respectively. Sample A2 was further annealed at 500 °C for 2 h in flowing Ar atmosphere. The annealed powder was labeled as sample A4. As comparison, the mixed solution containing $CoCl_2{\cdot}6H_2O$, $SnCl_2{\cdot}2H_2O$, $NaBH_4$ and de-ionized water with the same ratio as the preparation of other samples was directly filtered and washed without hydrothermal treatment, which was labeled as sample A0.

Metal Sn was also synthesized by hydrothermal route at 160 °C for 48 h, and the product was labeled as sample A5. The reactions employed here to form $CoSn_3$ alloy and metal Sn are described by reactions (1) and (2), respectively. The synthesis conditions for all the samples investigated in this work are listed in Table 1.

$$CoCl_2{\cdot}6H_2O + 3SnCl_2{\cdot}2H_2O + 8NaBH_4 \rightarrow CoSn_3 + 4B_2H_6\uparrow + 8NaCl + 4H_2\uparrow + 12H_2O \quad (1)$$

$$SnCl_2{\cdot}2H_2O + 2NaBH_4 \rightarrow Sn + B_2H_6\uparrow + 2NaCl + H_2\uparrow + 2H_2O \quad (2)$$

The synthesized Co–Sn powders were analyzed by X-ray diffraction (XRD) using a Rigaku D/MAX-RB diffractometer equipped with Cu Kα radiation (λ = 1.5406 Å) in the range of $2\theta = 10$–90°. The particle morphology was characterized by field-emission scanning electron microscopy (FESEM, SUPRA55) combined with energy dispersive spectra (EDS) analysis.

Galvanostatic cycling tests were performed in Swagelok cells assembled under Ar atmosphere, in a MIKROUNA glove box having O_2 and H_2O contents at ppm levels. The working electrode was formed as a thin film by spreading slurry out on a copper foil. The slurry was a mixture composed of 80 wt.% synthesized active materials, 10 wt.% PVDF as binder dissolved in N-methylpyrrolidinone (NMP), and 10 wt.% acetylene black as conductive agent. After NMP evaporation, the spread foil was cut into circular disks with 8 mm diameter and dried at 120 °C under vacuum for 24 h. The disk was used as the positive electrode and a lithium foil as the counter electrode. The electrolyte was 1 M $LiPF_6$ in a solvent mixture of ethylene carbonate (EC), methyl ethylene carbonate (MEC) and dimethyl carbonate (DMC) (1:1:1 by volume) soaked on a Celgard 2400 polypropylene separator. The galvanostatic cycling tests were performed within a 0.01–1.2 V voltage limit, using a LAND CT2001C battery test system (Wuhan, China).

3. Results and discussion

3.1. Effect of dwelling time on phase composition and electrochemical properties of hydrothermally synthesized Co–Sn alloy powders

The XRD pattern of sample A0 is shown in Fig. 1. Only Sn and $Sn_6O_4(OH)_4$ are detectable without any signal attributable to Co related phases. The coexistence of Sn and $Sn_6O_4(OH)_4$ can be elucidated by reactions (2) and (3) [12], respectively. Although metal Co is indiscernible in the XRD pattern, the reaction of Co reduced from $CoCl_2{\cdot}6H_2O$ by $NaBH_4$ can actually take place at room temperature. Therefore, the produced metal Co exists most probably in amorphous state, which is accounted for the mussy background peaks in Fig. 1. This also suggests that no alloying between Co and Sn occurs at room temperature.

$$6Sn^{2+} + 12OH^- \rightarrow 6Sn(OH)_2 \rightarrow Sn_6O_4(OH)_4 + 4H_2O \quad (3)$$

The impacts of reaction duration on the phase composition and the crystallinity of the precipitates prepared at 160 °C without heat-treatment were investigated. XRD patterns of samples with different reaction durations of 24 h, 48 h and 60 h are illustrated in Fig. 2(a), (b) and (c), respectively. Sn-based oxides and $CoSn_2$ (JCPDS Library 65-2697) alloy coexist in the three samples. The existence of Sn-based oxides can be ascribed to the decomposition of $Sn_6O_4(OH)_4$ to SnO under hydrothermal condition and then a part of SnO further oxidized in aerobic ambiance. When the dwelling

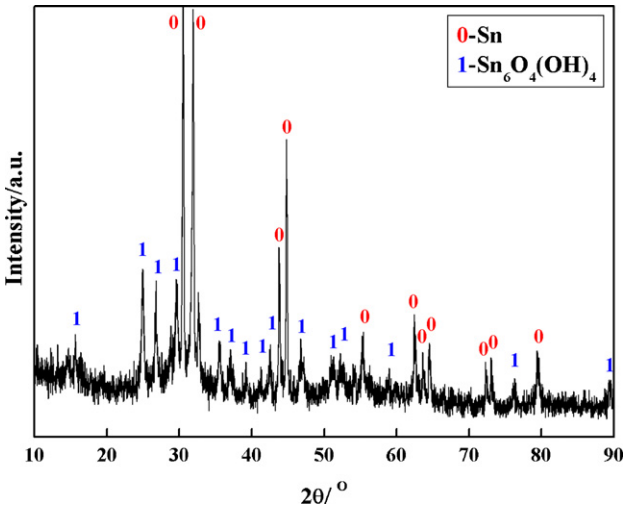

Fig. 1. XRD pattern of sample A0.

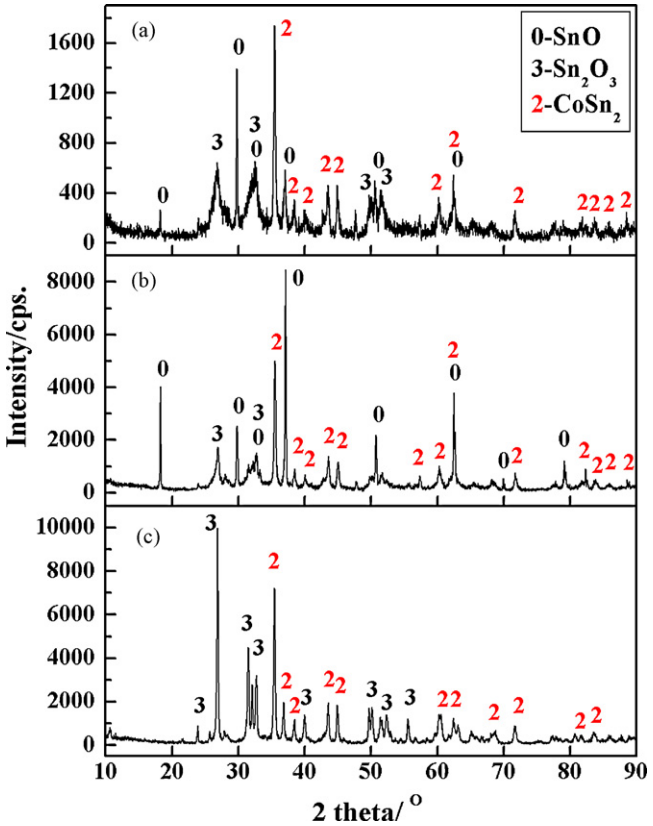

Fig. 2. XRD patterns of samples hydrothermally prepared at 160 °C for (a) 24 h (sample A1), (b) 48 h (sample A2) and (c) 60 h (sample A3).

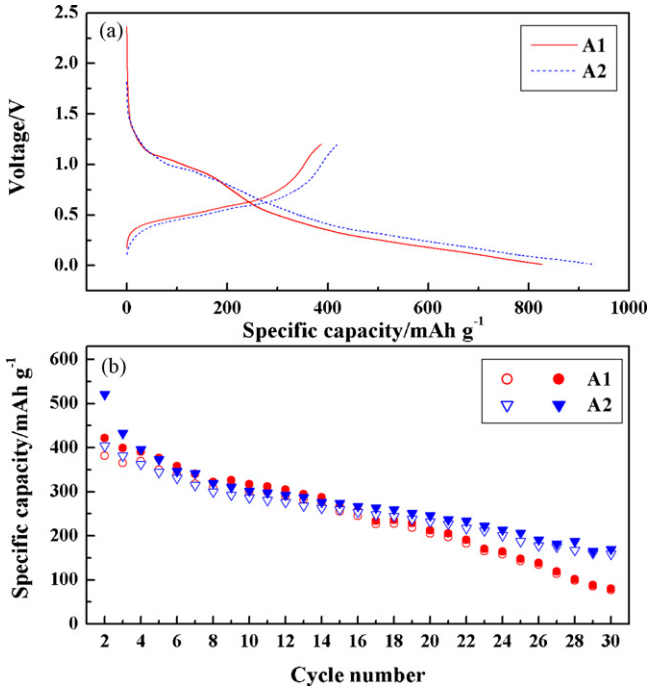

Fig. 3. Electrochemical performances of samples A1 and A2: (a) voltage profiles for the initial cycle and (b) cycling performance after the first cycle.

time is prolonged to 60 h, SnO is fully oxidized to Sn_2O_3. The presence of $CoSn_2$ alloy demonstrates that metal Co reduced from $CoCl_2{\cdot}6H_2O$ has alloyed with Sn under the hydrothermal conditions. Due to the formation of Sn-based oxides in the hydrothermal system, element Sn participating in alloying with Co is relatively deficient, resulting in the generation of $CoSn_2$ instead of the objective phase $CoSn_3$. The intensities of the peaks of Sn oxides and $CoSn_2$ are increasing as the reaction duration prolonged, suggesting that the prolongation of dwelling time can enhance the crystallinity of the precipitates. Moreover, the prolongation of reaction duration leads to the increase of average grain size of $CoSn_2$ phase in the samples, which are 24 nm, 26 nm and 33 nm for the samples A1, A2 and A3, respectively, according to the calculation by Scherrer equation.

The electrochemical performances of samples A1 and A2 are investigated, and the results are presented in Fig. 3. Due to the higher oxidation extent than that of samples A1 and A2, the cycling performance of sample A3 is not taken into account here. In this work, lithium insertion into anode electrodes is referred to as discharge and extraction as charge. As illustrated in Fig. 3(a), sample A2 displays a high first discharge capacity and a large irreversible capacity loss compared to sample A1. This is mainly attributed to the higher content of Sn oxides in sample A2 than that in sample A1. The plateau at ca. 1.0 V should correspond to the reaction of Li with Sn oxides. Li_2O, as irreversible reaction product, will be formed in the first lithiation process and a quite amount of lithium is thus consumed, causing a large initial lithiation capacity loss. In Fig. 3(b), after the initial 20 cycles, the reversible capacities of sample A1 decline faster than those of sample A2. This may be ascribed to the high content of Li_2O in sample A2, which, to some extent, can act as a buffer to accommodate the volume change of Sn during lithiation/delithiation process and thereby improve the cycling stability of electrodes. This strategy, forming Li_2O at the first lithiation process, has been accepted in Si-based electrode to buffer the huge volume change associated with alloying and dealloying of Si with Li, by using SiO as active material [13–16].

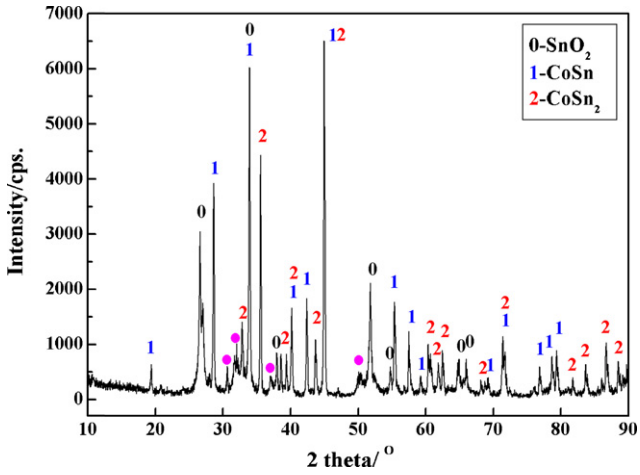

Fig. 4. XRD pattern of sample A4.

3.2. *Effect of annealing on the morphologies and the cycle performances of hydrothermally synthesized Co–Sn powders*

The XRD pattern of sample A4 after annealed at 500 °C for 2 h is displayed in Fig. 4. Sample A4 consists of SnO_2, CoSn and $CoSn_2$. Several unidentified peaks marked as solid circles may be other Sn oxides. The phases related to CoSn (JCPDS Library 65-3477) and $CoSn_2$ (JCPDS Library 65-2697) are hexagonal and tetragonal, respectively. The existence of SnO_2 can be ascribed to SnO and Sn_2O_3 produced during hydrothermal reaction fully oxidized in annealing process, which may be due to a small quantity of O_2 existing in the Ar atmosphere we used. The emergence of CoSn in the sample after heat-treatment is considered to be related to the thermal stability of $CoSn_2$. $CoSn_2$ will decompose to CoSn and Sn at 572 °C according to the Co–Sn binary phase diagram [17]. The nano-sized feature of $CoSn_2$ may lead to this decomposition at a lower temperature. The decomposed product of Sn with fresh surface will be oxidized to SnO_2 quickly at the annealing condition. According to the calculation by Scherrer equation, the average crystallite sizes of $CoSn_2$ in the annealed samples (ca. 60 nm) are larger than those in the unannealed ones (26 nm).

The morphologies of samples A2 and A4 were characterized by FESEM. As shown in Fig. 5(a)–(c), both of the two samples display two different morphologies, bubbles-like and whisker-like particles. EDS spot analysis profiles for the images of Fig. 5(b) and (c) are exhibited in Fig. 5(d) and (e), respectively. The particles in sample A2 are quite smaller than those in sample A4. In Fig. 5(d), Sn, Co, O and Cu elements are identified. The Cu peaks come from the copper foil to support the powders for FESEM analysis. The Co/Sn atomic ratio is 53.07:27.78, greatly exceeding the element ratio in CoSn and $CoSn_2$. This indicates that element Co reduced from $CoCl_2{\cdot}6H_2O$ does not fully alloy with the rest Sn which has not been oxidized. However, no peaks due to metal Co are found in the XRD pattern of sample A4 (Fig. 4), implying that Co exists in an amorphous state. Metal Co and SnO_2 mantle on the Co–Sn alloy grains, resulting in the ambiguous particles surface. No Co peaks can be discerned in Fig. 5(e), implying that the whisker-like particles are all the aggregates of SnO_2.

The electrochemical performances of the unannealed and annealed powders (samples A2 and A4, respectively) are investigated, and the results are illustrated in Fig. 6. The first discharge capacity of sample A2 is distinctly higher than that of sample A4, but after the initial cycle, the reversible capacities of sample A2 are rapidly declining, while those of sample A4 keep almost stable until the 20th cycle. The discrepancies of the cycling performance between samples A2 and A4 should be related to the different com-

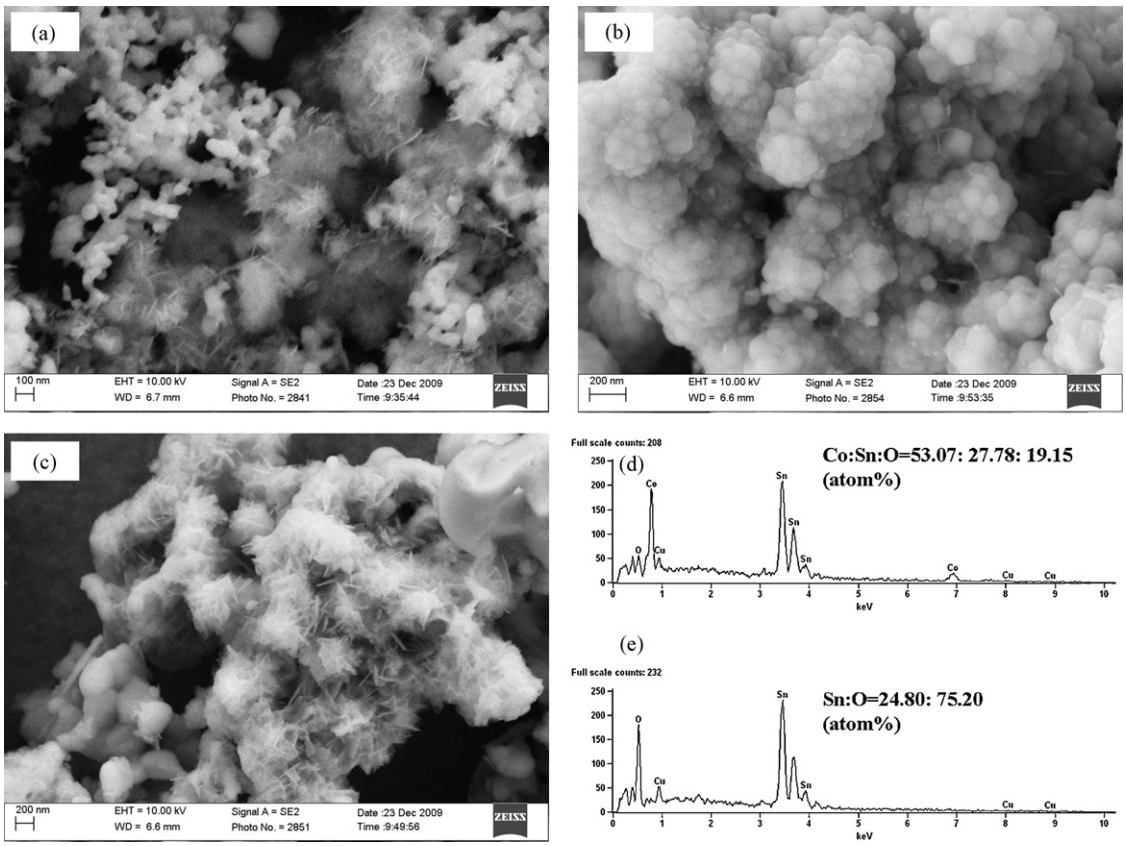

Fig. 5. FESEM images of (a) particle morphology of sample A2; (b) bubbles-like and (c) whisker-like particles in sample A4; (d) EDS spot analysis for the spherical grains shown in image (b); (e) EDS spot analysis for the whisker-like grains shown in image (c).

positions consisting in the samples, the ratios of the compositions and the particle sizes. The oxide state of Sn in sample A2 (SnO and Sn_2O_3) is lower than that in sample A4 (SnO_2). The relatively lower initial coulombic efficiency of sample A2 implies that the initial irreversible capacity does not mainly come from the irreversible reaction of Li^+ with Sn oxides (forming Li_2O), the smaller particle size and thus the high specific surface area of synthesized sample A2 should be accounted for the high irreversible capacity. High surface area usually corresponds to the formation of more SEI film, which consumes much Li^+ and results in high irreversible capac-

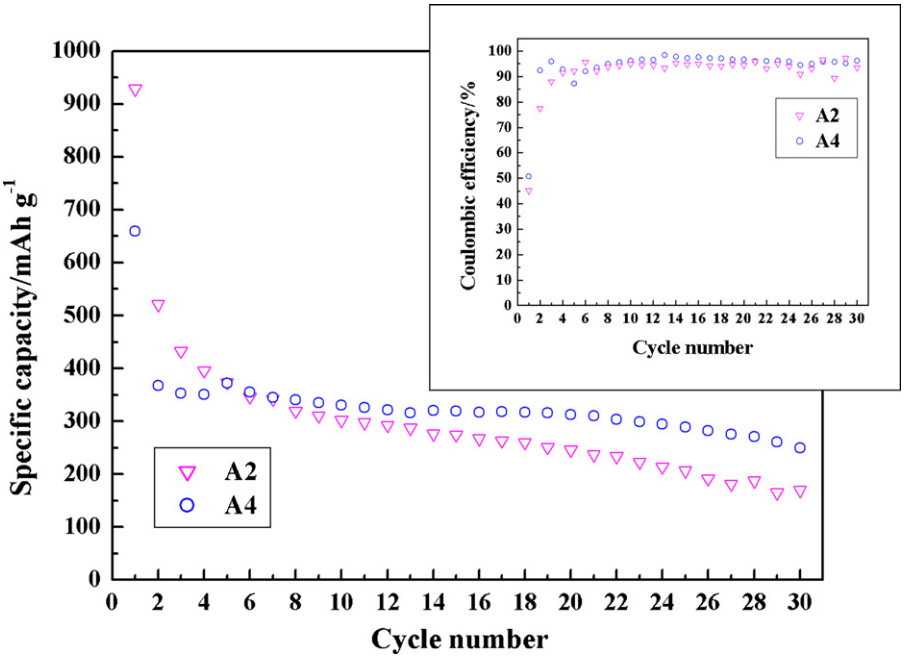

Fig. 6. Electrochemical cycling performances of samples A2 and A4 at current density of 100 mA/g.

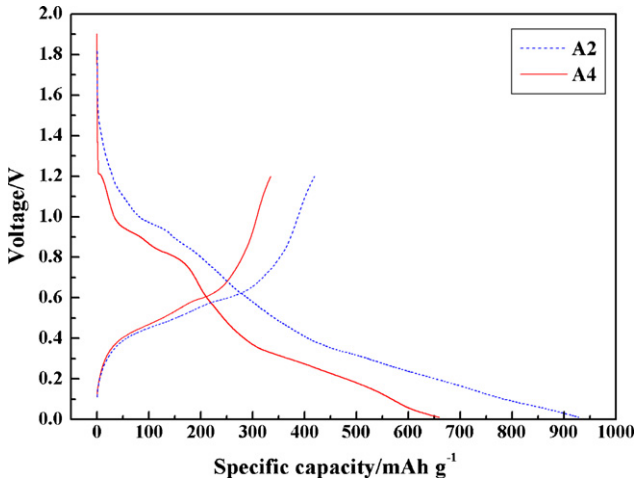

Fig. 7. Voltage profiles for the first cycle of samples A2 and A4 cycling at 100 mA/g.

ity. The better cycling stability of sample A4 may be related to the role of CoSn in absorbing the volume change of Li_xSn during lithiation and delithiation (pure CoSn produced via this process is electrochemically inert, which is not exhibited in this work). Sample A4 displays the reversible capacity around 300 mAh/g. Although its gravimetric specific capacity is close to that of graphite, its volumetric specific capacity is more than twice that of graphite because of the high density of sample A4 (above 7 g/cm^3). From this viewpoint, sample A4 is still a potential high capacity anode material for Li-ion batteries. However, the reversible capacity of sample A4 is gradually declining after 21 cycles. It is believed that a further improvement on cycling performance could be achieved after optimizing the electrode composition (the ratio among active material, binder and conductive agent) and the electrode film preparation technique.

Each of samples A2 and A4 shows an initial cycle profile typical of multi-phase reactions [18], as shown in Fig. 7. The voltage curves of both the samples intersect at around 0.6 V. This voltage represents the equipotential for the electrochemical reactions of the two samples in the first cycle. In Fig. 8(a), the equipotential points for the 2nd, 8th, 20th and 30th cycles of sample A2 are labeled in Fig. 8(c) as a1, b1, c1 and d1, respectively. Similarly, the equipotential points for sample A4 in Fig. 8(b) are labeled as a2, b2, c2 and d2 in Fig. 8(d). The relevant voltage values of all the equipotential points are listed in Table 2. For sample A2, the equipotential for lithiation/delithiation reactions in different cycles gradually decrease and is lower than the corresponding voltage for sample A4. This indicates that the polarization of lithiation process becomes much serious than that of the delithiation process for sample A2, and the lithiation into sample A2 becomes progressively more difficult than into sample A4. This can be partially responsible for the rapid capacity decline of sample A2. With respect to sample A4 for which the equipotential nearly keeps constant, the electrode polarization degree for lithiation and delithiation processes is almost the same, suggesting the similar lithiation/delithiation kinetic process. However, to each of samples A2 and A4, the equilibrium voltage for the 2nd cycle is much lower than that for the initial cycle. We speculate that after the first cycle, both of the samples encounter irreversible reactions resulting in the emergence of some poor-conductive substances (e.g. Li_2O) and the structure transformation of the active materials.

Table 2
The equipotential values in the voltage curves for samples A2 and A4 as indicated in Fig. 8 (c) and (d).

Point	a1	b1	c1	d1	a2	b2	c2	d2
Voltage/*V*	0.433	0.417	0.407	0.386	0.434	0.423	0.421	0.425

3.3. Lithiation/delithiation mechanism of $CoSn_2$ alloy

In order to clarify the lithiation/delithiation mechanism of $CoSn_2$, as reference, sample A5 with nominal composition of pure Sn is synthesized under the identical condition with sample A2. Fig. 9 presents the XRD pattern of sample A5. Besides the predominant phase of crystallite metal Sn, SnO impurity is also formed unavoidably.

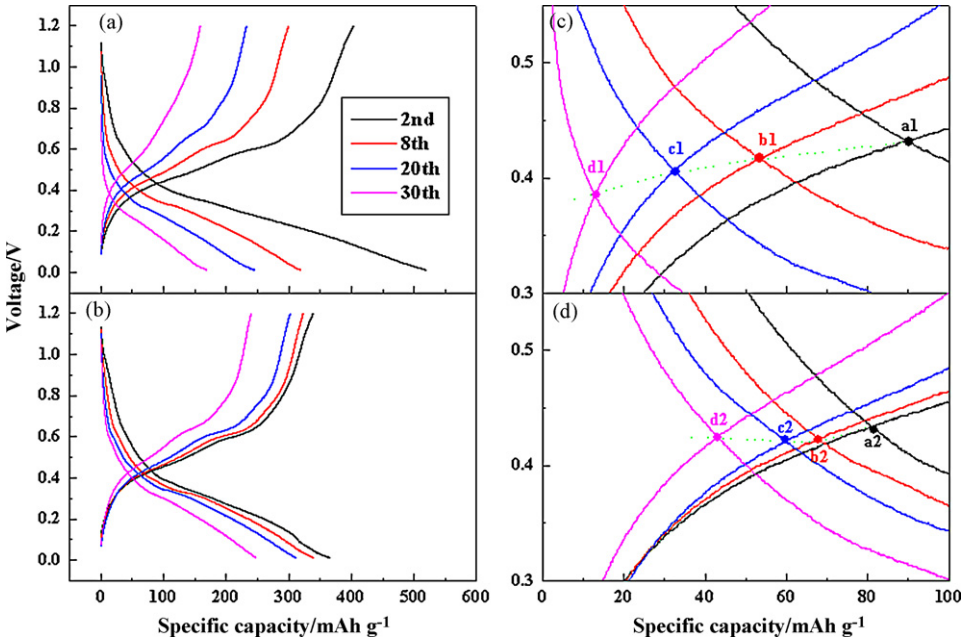

Fig. 8. Voltage profiles for the 2nd, 8th, 20th and 30th cycles of (a) sample A2 and (b) sample A4 cycling at 100 mA/g; profiles (c) and (d) corresponding to the local magnification of profiles (a) and (b), respectively.

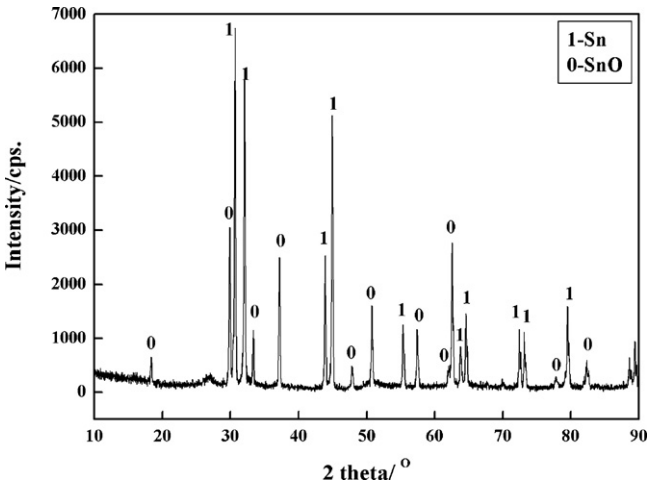

Fig. 9. XRD pattern of the nominal Sn.

The lithiation/delithiation processes of samples A2 and A5 were characterized in Fig. 10. The cycling current density was 100 mA/g. In the first cathodic scan, for sample A5, the first peak around 1.3 V in Fig. 10(a) is quite likely associated to the decomposition of the electrolyte and the formation of the SEI film on the electrode surface. Lithium insertion into SnO_2 to form Sn has been reported at around 1.0 V [19], so it is reasonable to speculate that the cathodic peak around 0.85 V, which is indiscernible in Fig. 10(b), should be related to the irreversible reaction of SnO with Li^+, followed by the formation of Li_xSn alloys below 0.8 V. For sample A2, the cathodic peaks at 0.96 V and 0.85 V result from the reactions of Sn_2O_3 and SnO with Li^+, respectively. The cathodic peak at 0.37 V and the corresponding anodic peak at 0.6 V are corresponding to the potential plateau of lithiation and delithiation reaction of metal Sn,

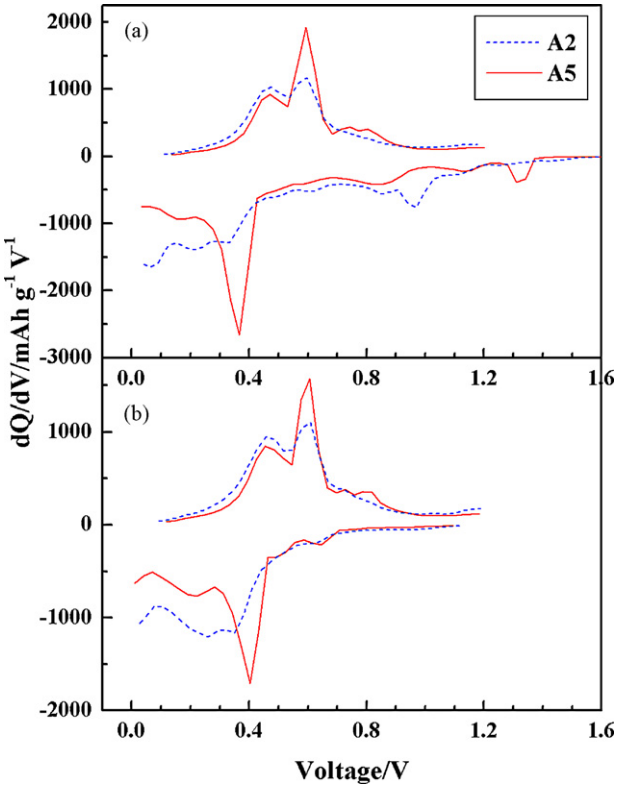

Fig. 10. Differential capacity curves of samples A2 and A5 for (a) the 1st cycle and (b) the 2nd cycle.

respectively. The electrochemical reaction at 0.37 V is related to the formation of Li_xSn ($x = 3.5$), which is slightly lower than the equilibrium potential (0.42 V) of $Li_{3.5}Sn$ [19,20] due to the electrode polarization. The intensities of the cathodic peak at 0.37 V and the anodic peak at 0.6 V are much higher for sample A5 than those of sample A2, indicating the high crystallinity of Sn in sample A5. However, the Sn derived from Sn oxides (SnO and Sn_2O_3) and $CoSn_2$ in the initial lithiation process for sample A2 has a poor crystallinity, which leads to the broad redox peaks for lithiation and delithiation of Sn.

In the first two cycles, two distinguished anodic peaks, observed at around 0.47 V and 0.60 V for both samples A2 and A5, should result from the dealloying reaction of $Li_{22}Sn_5$ and Li_7Sn_2, respectively. Except for the first cathodic scan curve, very similar profiles are observed for samples A2 and A5. Consequently, a two-step lithiation/delithiation mechanism for electrochemical reaction of $CoSn_2$ alloy with Li^+ is proposed, involving an irreversible substitution of Co out of $CoSn_2$ alloy in the first lithiation process and a classical dealloying/alloying reaction of Li_xSn in the following cycles. The mechanism can be briefly expressed by Eqs. (4) and (5) [21], although different mechanism is proposed in literature [22].

$$CoSn_2 + 2xLi^+ + 2xe^- \rightarrow Co + 2Li_xSn \quad (4)$$

$$Li_xSn \leftrightarrow xLi^+ + xe^- + Sn \quad (5)$$

4. Conclusion

Co–Sn alloys are difficult to be synthesized at room temperature from aqueous solution by $NaBH_4$ reduction. Hydrothermal treatment can enhance the alloying process between Co and Sn, and the synthesized phases and thus the corresponding electrochemical properties strongly depend on the processing conditions. The prolongation of dwelling time in hydrothermal process readily results in the generation of more Sn oxides, and thus causing a higher first discharge capacity and a larger initial irreversible capacity loss. On the other hand, the irreversible product Li_2O resulted from the initial reaction between Sn oxides and Li^+ can act as a buffer component to improve the cycle life of electrodes to some extent. However, too long dwelling time causes excessive Sn oxides and thus deteriorates the electrochemical performance of electrode. Annealing treatment increases the crystallinity of the hydrothermally synthesized Co–Sn alloys and causes the emergence of a certain amount of inert CoSn, and thus favorable for the increase of initial coulombic efficiency and the improvement of cycling stability of electrode. By compared to the lithiation/delithiation processes of metal Sn, a two-step electrochemical reaction mechanism of $CoSn_2$ alloy with Li^+ is confirmed.

Acknowledgments

This research work has been performed with the financial support of 863 Program of National High Technology Research Development Project of China (No. 2006AA43Z231), Program for Guangdong Industry-Academy-Alliance Research (No. 2009A090100020) and Program for New Century Excellent Talents in University of China (No. NCET-07-0072).

References

[1] G. Mulas, S. Enzo, C. Bonatto Minella, E. Arca, C. Gerbaldi, N. Penazzi, S. Bodoardo, J. Hassoun, S. Panero, J. Solid State Electrochem. 13 (2009) 239–243.
[2] J.O. Besenhard, M. Wachtler, M. Winter, R. Andreaus, I. Rom, W. Sitte, J. Power Sources 81–82 (1999) 268–272.
[3] H. Li, L. Shi, Q. Wang, L. Chen, X. Huang, Solid State Ionics 148 (2002) 247–258.
[4] J. Xie, X.B. Zhao, G.S. Cao, J.P. Tu, J. Power Sources 164 (2007) 386–389.
[5] R. Alcántara, U. Nwokeke, I. Rodríguez, J.L. Tirado, Electrochem. Solid-State Lett. 11 (2008) A209–A213.
[6] R. Alcántara, I. Rodríguez, J.L. Tirado, Chem. Phys. Chem. 9 (2008) 1171–1177.

[7] F. Nacimiento, R. Alcántara, J.L. Tirado, J. Alloys Compd. 485 (2009) 385–390.
[8] C.Q. Zhang, J.P. Tu, X.H. Huang, Y.F. Yuan, S.F. Wang, F. Mao, J. Alloys Compd. 457 (2008) 81–85.
[9] Z. Wang, W. Tian, X. Liu, R. Yang, X. Li, J. Solid State Chem. 180 (2007) 3360–3365.
[10] A. Trifonova, M. Wachtler, M.R. Wagner, H. Schroettner, Ch. Mitterbauer, F. Hofer, K.C. Möller, M. Winter, J.O. Besenhard, Solid State Ionics 168 (2004) 51–59.
[11] F.S. Ke, L. Huang, H.B. Wei, J.S. Cai, X.Y. Fan, F.Z. Yang, S.G. Sun, J. Power Sources 170 (2007) 450–455.
[12] K. Lin, X. Wang, Y. Xu, Chin. J. Power Sources 129 (2005) 508–510.
[13] C.H. Doh, C.W. Park, H.M. Shin, D.H. Kim, Y.D. Chung, S.I. Moon, B.S. Jin, H.S. Kim, A. Veluchamy, J. Power Sources 179 (2008) 367–370.
[14] T. Kim, S. Park, S.M. Oh, J. Electrochem. Soc. 154 (2007) A1112–A1117.
[15] C.H. Doh, H.M. Shin, D.H. Kim, Y.C. Ha, B.S. Jin, H.S. Kim, S.I. Moon, A. Veluchamy, Electrochem. Commun. 10 (2008) 233–237.
[16] J.H. Kim, H.J. Sohn, H. Kim, G. Jeong, W. Choi, J. Power Sources 170 (2007) 456–459.
[17] G.P. Vassilev, K.I. Lilova, J.C. Gachon, Intermetallics 15 (2007) 1156–1162.
[18] L. Huang, J.S. Cai, Y. He, F.S. Ke, S.G. Sun, Electrochem. Commun. 11 (2009) 950–953.
[19] C. Wang, A. John Appleby, F.E. Little, J. Power Sources 93 (2001) 174–185.
[20] R.A. Huggins, J. Power Sources 81–82 (1999) 13–19.
[21] M. Xue, Z. Fu, Solid State Ionics 177 (2006) 1501–1507.
[22] N. Tamura, M. Fujimoto, M. Kamino, S. Fujitani, Electrochim. Acta 49 (2004) 1949–1956.